

SCIENTIFIC REPORTS



OPEN

Fastest Formation Routes of Nanocarbons in Solution Plasma Processes

Tetsunori Morishita¹, Tomonaga Ueno^{1,2,3}, Gasidit Panomsuwan², Junko Hieda¹, Akihito Yoshida¹, Maria Antoaneta Bratescu¹ & Nagahiro Saito^{1,2,3}

Received: 18 August 2016

Accepted: 24 October 2016

Published: 14 November 2016

Although solution-plasma processing enables room-temperature synthesis of nanocarbons, the underlying mechanisms are not well understood. We investigated the routes of solution-plasma-induced nanocarbon formation from hexane, hexadecane, cyclohexane, and benzene. The synthesis rate from benzene was the highest. However, the nanocarbons from linear molecules were more crystalline than those from ring molecules. Linear molecules decomposed into shorter olefins, whereas ring molecules were reconstructed in the plasma. In the saturated ring molecules, C–H dissociation proceeded, followed by conversion into unsaturated ring molecules. However, unsaturated ring molecules were directly polymerized through cation radicals, such as benzene radical cation, and were converted into two- and three-ring molecules at the plasma–solution interface. The nanocarbons from linear molecules were synthesized in plasma from small molecules such as C₂ under heat; the obtained products were the same as those obtained via pyrolysis synthesis. Conversely, the nanocarbons obtained from ring molecules were directly synthesized through an intermediate, such as benzene radical cation, at the interface between plasma and solution, resulting in the same products as those obtained via polymerization. These two different reaction fields provide a reasonable explanation for the fastest synthesis rate observed in the case of benzene.

Liquid-phase plasma^{1–5} has attracted the attention of several researchers engaged in plasma science, especially for applications involving materials and water treatment^{6–10}. The properties of liquid-phase and atmospheric plasmas differ even though liquid-phase plasma is a particular type of atmospheric plasma. Several types of liquid-phase plasma, e.g., streamer, spark, arc, and glow discharge plasmas, and their various formation methods have been reported^{11–14}. We have already demonstrated a spark–glow transition plasma in aqueous solution and have used it to fabricate gold nanoparticles in the absence of a reducing agent^{15–24}. This plasma is named solution plasma. It is a non-equilibrium plasma in solution, and the characteristics of plasma and solution are coupled by the exchange of electrons and ions.

Solution plasma can potentially be used for the precise nanomaterial synthesis. In general, the electron temperature is higher than the ion temperature in the case of non-equilibrium plasma²⁵. However, the temperature at the center of the plasma is still high, i.e., approximately 4000 K^{26,27}, even though the solution temperature is maintained at approximately room temperature. Thus, a temperature gradient exists between the center of the plasma and the plasma–solution interface. This temperature gradient is extremely large because the plasma is surrounded by liquid as a condensed phase. The activated particles, including ions, electrons, radicals, and photons, are quenched and then deactivated. However, such species have sufficient energy to induce precise chemical reactions but not physical changes. Unique reactions can thereby occur at the interface under room temperature. Various researchers have used the solution plasma to synthesize Au, Pt²⁸, AuPt²⁹, Pd³⁰, PdAu³¹, Ag³², Au alloys^{33,34}, metal oxide nanoparticles^{35–38}, and nanosheets^{39–41}. It has also been used to modify the surface of carbon materials to achieve monodispersion⁴², to prepare metal nanoparticles on carbon^{43–46}, and to degrade gelatin⁴⁷, among other applications^{48–59}.

¹Department of Material Science and Engineering, Graduate School of Engineering, Nagoya University, Furo-cho, Chikusa-ku, Nagoya, 464-8603, Japan. ²NU- PPC Plasma Chemical Technology Center, The Petroleum and Petrochemical College, Chulalongkorn University, Bangkok 10330, Thailand. ³CREST, JST, Furo-cho, Chikusa-ku, Nagoya, 464-8603, Japan. Correspondence and requests for materials should be addressed to N.S. (email: hiro@rd.numse.nagoya-u.ac.jp)

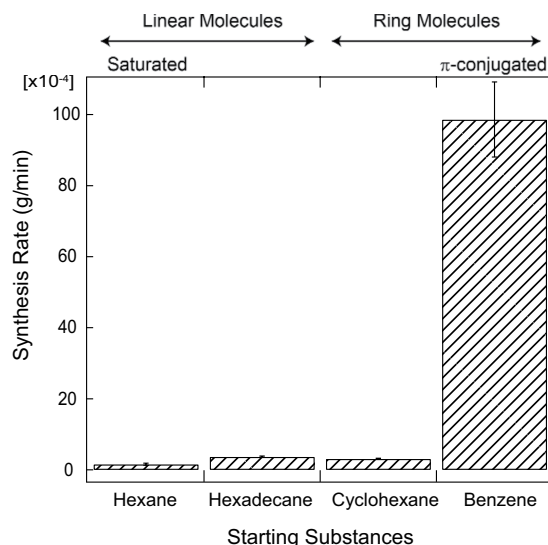


Figure 1. Synthesis rates of nanocarbons from hexane, hexadecane, cyclohexane, and benzene.

Recently, we attempted to adapt the solution plasma system to organic solutions (see Supplementary video and Fig. 1S). In such systems, the plasma enables unique reactions such as C–H activation reactions at the interface between the solution and plasma, whereas conventional plasma induces random decomposition reactions. We have fabricated graphene, heterographene, nanocarbon sheets, and nanocarbon spheres via solution plasma from organic solutions containing solvents such as benzene, toluene, pyridine, or pyrazine^{60–72}. Moreover, the reaction rate is substantially higher than the rates of other synthesis methods such as chemical vapor deposition and pyrolysis synthesis. However, solution plasma is a relatively new process and the knowledge accumulated thus far is insufficient to enable the design and control of the processes and products.

There are two reaction routes from solution, i.e., routes from starting substances to products. The first is the reaction route through plasma, which is composed of the vaporized solution and decomposed species and where the gas temperature approaches 4000 K. The second is the reaction route at the interface between the plasma and solution, where the ion temperature is as low as room temperature, but the electron temperature is still sufficient to advance the organic reaction. Nanocarbons might form at this interface because the structure and composition of the product are inherited from the starting substances. If the reaction in plasma is the main route, the product structure and composition will become random and complex. However, the details of reaction mechanism are not known.

In this study, the nanocarbon formation routes via the solution plasma process were investigated. To simplify the reaction routes for synthesizing nanocarbons, we used starting materials categorized as either linear or ring molecules. The products were analyzed by gas chromatography–mass spectrometry (GC/MS), X-ray diffraction (XRD), Raman spectrometry, and *ab initio* MO calculations. The intermediates involved in the conversion of the starting materials to nanocarbon products were estimated; the nanocarbon formation routes are discussed.

Results and Discussion

Nanocarbons were synthesized using solution plasma from hexane, hexadecane, cyclohexane, and benzene. The synthesized nanocarbons were collected, and the synthesis rates of the nanocarbons were estimated. Figure 1 shows the synthesis rates of nanocarbons from hexane, hexadecane, cyclohexane, and benzene. The respective synthesis rates of nanocarbons were 1.6×10^{-4} , 3.7×10^{-4} , 3.1×10^{-4} , and 98.6×10^{-4} g/min. The synthesis rates of nanocarbons obtained from linear molecules, i.e., hexane and hexadecane, were obviously lower than that of nanocarbons obtained from ring molecules, i.e., benzene. In particular, the synthesis rate of nanocarbon from benzene was substantially greater than that of nanocarbons from the other investigated solvent. This result means that the π -conjugated bonds in a ring structure enhanced nanocarbon synthesis in the case of solution plasma.

To characterize the carbon structure synthesized from linear and ring molecules, XRD and Raman spectra of the hexane, hexadecane, cyclohexane, and benzene systems were collected; the results are shown in Figs 2 and 3. The XRD patterns of all nanocarbons show broad peaks around $2\theta = 24^\circ$ corresponding to the (002) plane of graphite. These peaks are different by the molecule and the calculated lattice spacing of hexane, hexadecane, cyclohexane, and benzene were 0.357, 0.371, 0.365, and 0.386 nm, respectively. Lattice spacing of hexane is closer to that of highly oriented pyrolytic graphite. It means the crystallinity of nanocarbon synthesized from hexane is higher than that from benzene. In Raman spectra, the D- and G-bands appeared at 1350 and 1600 cm^{-1} , respectively. The D-band originates from the mixing of sp^3 orbitals in a plane with structural defects and/or impurities, whereas the G-band originates from the graphite structure. The ratio between the intensities of the D- and G-bands, $I(D)/I(G)$, is a crystallinity index for graphite because $I(D)/I(G) = 0$ for single-crystalline graphite. The $I(D)/I(G)$ ratio for the nanocarbon prepared from hexane and hexadecane were 0.933 and 0.894, whereas that for the nanocarbon prepared from cyclohexane and benzene were 0.978 and 0.984. Thus, the crystallinity of the nanocarbons synthesized from linear molecules is greater than that of nanocarbons synthesized from the

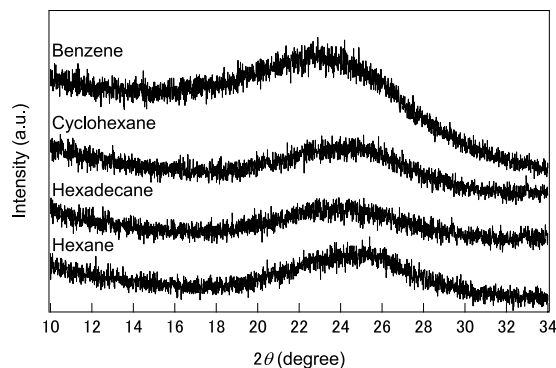


Figure 2. XRD patterns of the nanocarbons obtained from hexane, hexadecane, cyclohexane, and benzene.

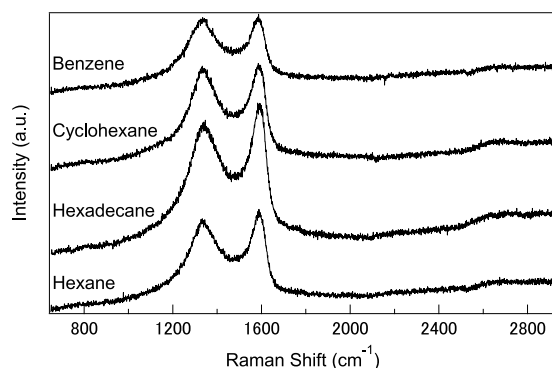


Figure 3. Raman spectra of the nanocarbons obtained from hexane and benzene.

corresponding ring molecules, although the synthesis rate of nanocarbons obtained from π -conjugated ring molecules is higher than that of nanocarbons prepared from linear molecules.

Figure 4 shows the GC/MS qualitative analysis results for the products synthesized from hexane, hexadecane, cyclohexane, and benzene. Figures 5 and 6 list the products of the linear and ring structures, with symbolic numbers L1)–L15) and R1)–R34) corresponding to the peaks in the GC/MS spectrogram. The products from the linear molecules were as follows. The products synthesized from hexane were R1), R2), R6), R8)~R13), R16) and R17). The products synthesized from hexadecane were L1)~L15). The products from the ring molecules were as follows. The products synthesized from cyclohexane were R3)~R14) and R16)~R19). Finally, the products synthesized from benzene were R3), R4), R6), R9)~R13) and R15)~R34).

Among the products of the syntheses starting from the linear molecules, small linear molecules and one- or two-ring molecules were observed. Specifically, molecules with one or two rings appeared in the product obtained from hexane, and the parts of rings molecules tend to be converted into π -conjugated ring molecules. Meanwhile, shorter olefins were observed in the product obtained from hexadecane. The peak intensities of the shorter olefins were greater than those of the longer ones. This product tendency was attributed to byproducts by the plasma decomposition. Oppositely, one- to six-ring molecules appeared in the products obtained from the synthesis of the ring molecules. A comparison of the peak intensities reveals that one-ring molecules tend to be directly converted into two- and/or three-ring molecules, not converted through smaller olefins.

Optical emission spectroscopy (OES) was performed to elucidate the relation between the states of plasma and the obtained products. Figure 7 shows the OES spectra for plasma formed from hexane, hexadecane, cyclohexane, and benzene. For all OES spectra, H_{α} , H_{β} , and C_2 lines were observed. The ratios of the peak intensities were approximately the same. Moreover, the background shapes were roughly the same. These results indicate that the plasma temperature was approximately uniform at the plasma center. From the blackbody radiation approximation, the plasma temperature at the center was approximately 4000–5000 K, according to Wien's displacement law. Such temperatures are sufficient to form graphite via organic compound decomposition.

Two reaction paths from monomer to polycyclic aromatic hydrocarbons (PAHs), including graphene, are shown in Fig. 8. One reaction path (reaction path 1) is from the plasma center. The solution is vaporized by a strong electric field between electrodes. The vaporized solution forms a gas phase between the electrodes, and the gas phase is converted into plasma after breakdown. In the plasma, organic compounds were almost completely decomposed, similar to the products obtained via pyrolysis synthesis. Meanwhile, the OES results indicate that H atoms and C_2 molecules were the main products at the plasma center. C_2 molecules undergo association reactions, i.e., carbonization, under the higher temperatures of approximately 4000–5000 K. Finally, the overall reaction provides graphite, graphene, and carbon-related materials⁷³. By contrast, C_2 molecules were generated at the interface between the plasma and solution. The temperature around the interface remained closer to the

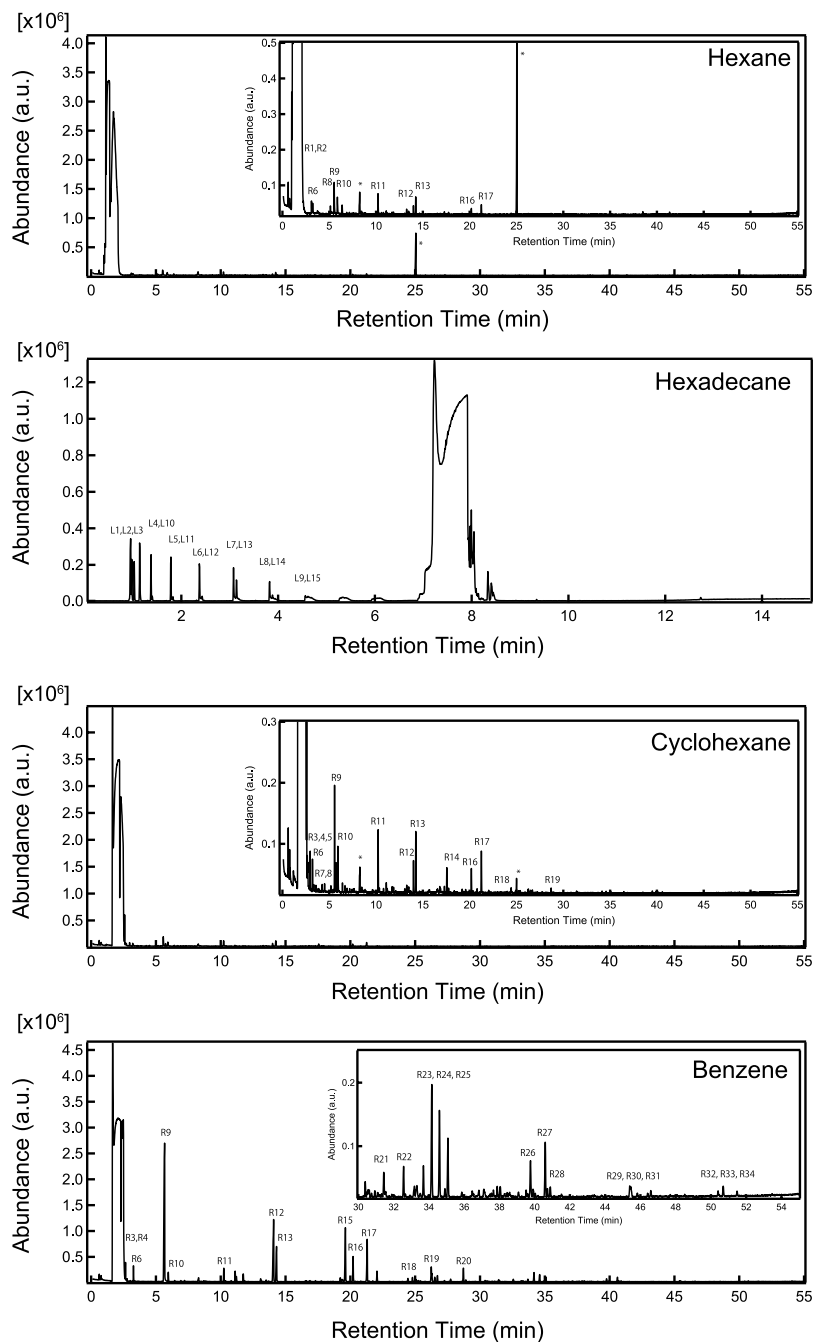


Figure 4. GC/MS qualitative analysis of the products synthesized from hexane, hexadecane, cyclohexane, and benzene. The peak labels correspond to the labels in Figs 5 and 6.

solution temperature. These C_2 molecules might exist as C_2H_2 and/or C_2H_4 because hydrogenation can occur at such temperatures. These molecules react with the main molecules into the solution—in our case, hexane, hexadecane, cyclohexane, and benzene—and the main molecules are associated or polymerized. The other reaction route is through the interface between the plasma and solution, where the temperature is sufficiently low. Non-equilibrium plasma in the liquid phase, such as solution plasma, requires secondary electrons to maintain the plasma state because it lacks electrons. In general, secondary electrons are supplied from electrodes, as they are frequently composed of metals. In the case of solution plasma, the solution component also functions as electrodes (i.e., liquid electrodes)^{1,2,4,5,74,75}, enabling the plasma to gain secondary electrons from the solution, i.e., molecules. Upon the emission of the secondary electrons, radical cations form into the solution. In the case of the solution where the formation of this radical cation preferentially occurs, this reaction path (reaction path 2) is favored over reaction path 1 because the volume of plasma is small. In the reaction path 2, the organic compounds and/or monomer are polymerized without the decomposition involved in the reaction path 1.

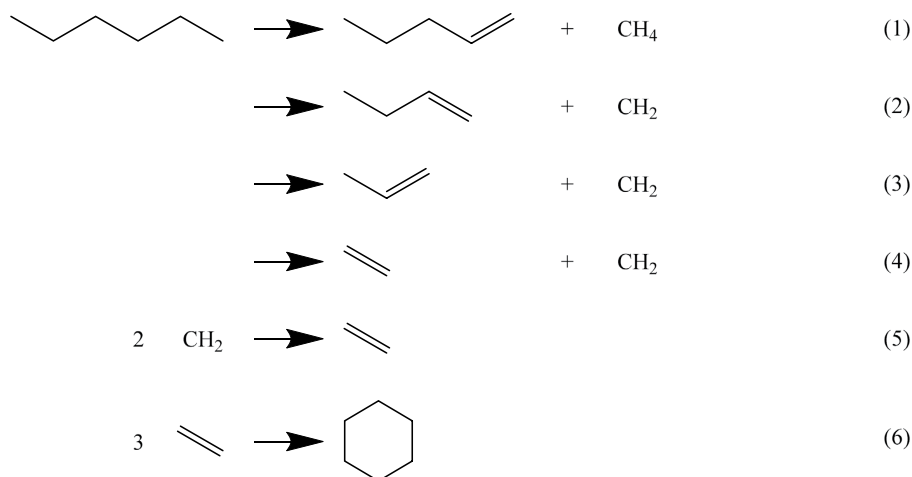
C numbers	Structures with Symbolic Numbers for Linear Molecules	
C4	L1) 1-Butene	
C5	L2) 1-Pentene	
C6	L3) 1-Hexene	
C7	L4) 1-Heptene	L10) Heptane
C8	L5) 1-Octene	L11) Heptane
C9	L6) 1-Nonene	L12) Nonane
C10	L7) 1-Decene	L13) Decane
C11	L8) 1-Undecene	L14) Undecane
C12	L9) 1-Dodecene	L15) Dodecane

Figure 5. The products obtained from the linear structures with symbolic numbers corresponding to the GC/MS spectrograms in Fig. 4.

When the linear molecules were used as starting materials, the synthesis rates were smaller than those of ring molecules and the products were more crystalline than those of ring molecules. These results indicate that the nanocarbon products obtained from the linear molecules are synthesized through the plasma center, which results in a greater crystallinity of the products compared to those obtained from the ring molecules. The $I(D)/I(G)$ ratios in the Raman spectra of the products obtained from the linear molecules such as hexane are lower than those of the products obtained from the ring molecules, although the ratios of the products obtained from linear molecules slightly vary. When the ring molecules were used as starting materials, the synthesis rate was higher than that when the linear molecules were used. The reaction rate has been particularly fast in the case of benzene. The expected intermediate, benzene radical cations, easily formed because of the presence of delocalized unsaturated bonds, i.e., π -conjugated orbitals. This benzene radical cation is known to be an important intermediate to polycyclic aromatic hydrocarbon (PAH)^{76–86}. The solution plasma can induce benzene radical cation formation even though this formation typically requires dedicated catalysts.

To discuss the formation of radical cations, we predicted the density of states of hexane, hexadecane, cyclohexane, and benzene using *ab initio* MO calculations, as shown in Fig. 9 (and Fig. 2S).

In Fig. 9, π -bonding and π -antibonding orbitals, σ -bonding and σ -antibonding orbitals of C–H, and σ -bonding and σ -antibonding orbitals of C–C are described by their respective contributions. The calculation results indicate that in the case of the linear molecules, the C–C bonds and C–H bonds will be decomposed in the plasma—not at the interface—because they are strongly stabilized. Specifically, the highest occupied molecular orbital (HOMO) and lowest unoccupied molecular orbital (LUMO) of hexane indicate that C–H dissociation and/or C–H and C–C dissociation at the tail end of chains are the primary reactions (see Fig. 2S). The GC/MS results for the product obtained from hexane show that the primary reactions proceed via thermal reactions in the plasma at the early stage of the following reactions (1)–(6):



In the case of hexadecane, the HOMO and LUMO indicate that the primary reactions of C–C dissociation of at the tail end, followed by C–H dissociation occur as secondary reactions (see Fig. 2S). In the case of hexadecane, shorter olefins were produced, whereas ring molecules were not observed. A longer discharge treatment will produce ring molecules such as cyclohexane. The HOMO and LUMO of cyclohexane indicate that C–H dissociation

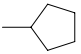
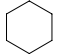
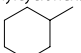
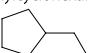
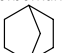
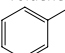
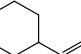
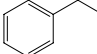
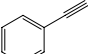
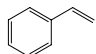
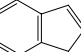
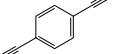
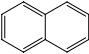
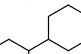
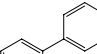
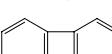
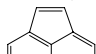
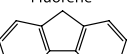
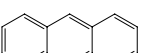
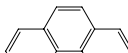
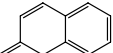
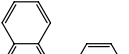
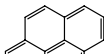
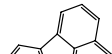
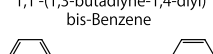
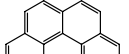
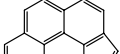
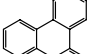
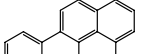
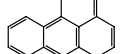
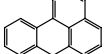
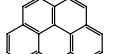
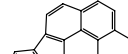
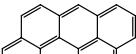
C numbers		Structures with Symbolic Numbers for Ring Molecules				
C6	R1)	Methylcyclopentane 	R2)	Cyclohexane 		
	R3)	Methylcyclohexane 	R4)	Ethylcyclohexane 	R5)	Norbornane 
C7					R6)	Toluene 
	R7)	Ethylcyclohexane 	R8)	Ethylbenzene 	R9)	Phenylethyne 
C8					R10)	Styrene 
	R11)	Indene 				
C9						
	R12)	1,4-Diethynylbenzene 	R13)	Naphthalene 		
C10						
	R14)	1,1'-Bicyclohexyl 	R15)	Biphenyl 	R16)	Biphenylene 
C12					R17)	Acenaphthylene 
C13	R18)	Fluorene 				
	R19)	Anthracene 	R20)	Phenanthrene 		
C14						
	R21)	4H-Cyclopenta[def]phenanthrene 				
C15						
	R22)	1-phenyl-Naphthalene, 	R23)	Pyrene 	R24)	Fluoranthene 
C16					R25)	1,1'-(1,3-butadiyne-1,4-diyl) bis-Benzene 
C18	R26)	Benzo[ghi]fluoranthene 	R27)	Cyclopenta[cd]pyrene 	R28)	Triphenylene 
	R29)	Benzo[a]pyrene 	R30)	Benzo[e]pyrene 	R31)	Perylene 
C20						
	R32)	Benzo[ghi]perylene 	R33)	Indeno[1,2,3-cd]pyrene 	R34)	Dibenzo[def,mno]chrysene 
C22						

Figure 6. The products obtained from the ring structures with symbolic numbers corresponding to the GC/MS spectrograms in Fig. 4.

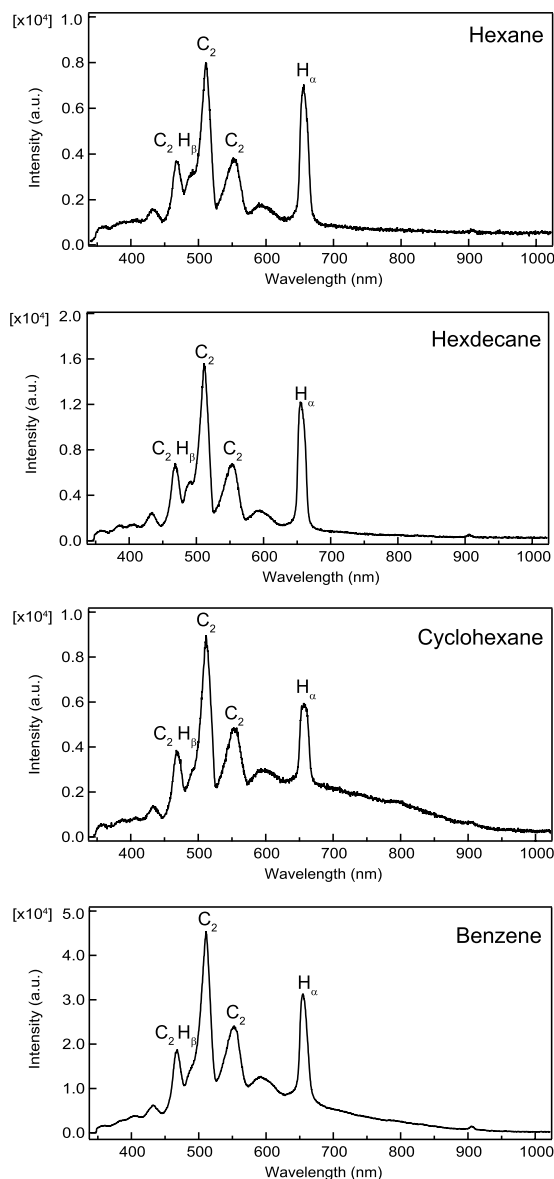
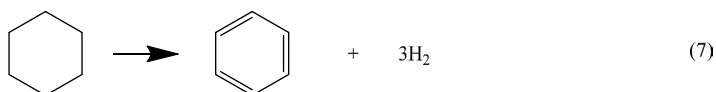


Figure 7. Optical emission spectra for plasmas formed in hexane, hexadecane, cyclohexane, and benzene.

proceeds as the primary reaction, which leads to unsaturated ring molecules such as benzene (see Fig. 2S). Furthermore, activated carbon materials function as catalysts for the dehydrogenation reaction of cyclohexane⁸⁷. In our reaction system, the synthesized carbons can enhance the following dehydrogenation reaction:



Oppositely, in the case of benzene, π -conjugated bonding and antibonding orbitals are closer to the Fermi level, i.e., benzene exhibits greater reactivity. The electrons in π -orbitals are easily excited to π^* orbitals because of the plasma sheath potential, which is the same as the electrical double-layer potential in electrochemical reactions. Furthermore, the excited electrons are emitted by collisions of particles, including ions and electrons, at the interface. Benzene radical cations will be formed at the interface through the excitation and emission of electrons (see the reaction (8)). These cations are considered an important intermediate in the formation of PAHs, i.e., nanocarbons. Benzene radical cations are converted into biphenyl and then into triphenylene as the following reactions (8)–(11):

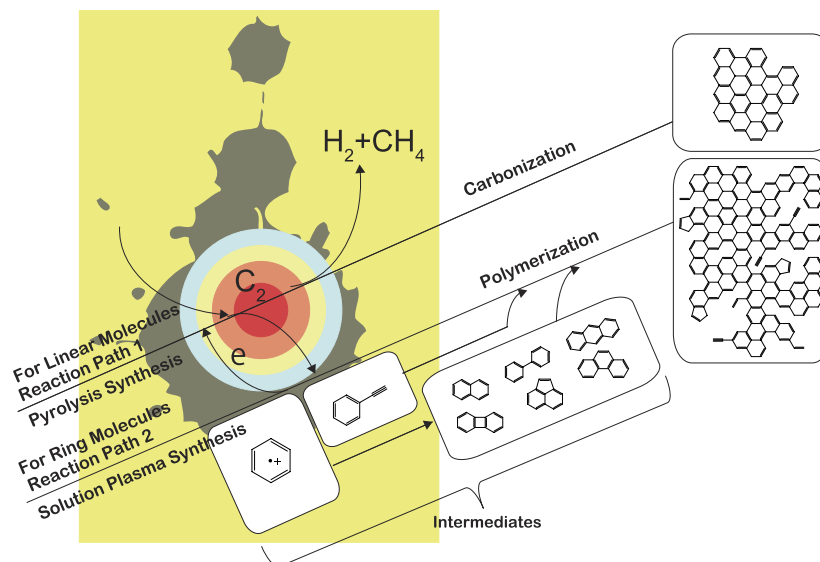


Figure 8. Reaction routes from hexane, hexadecane, cyclohexane, and benzene.

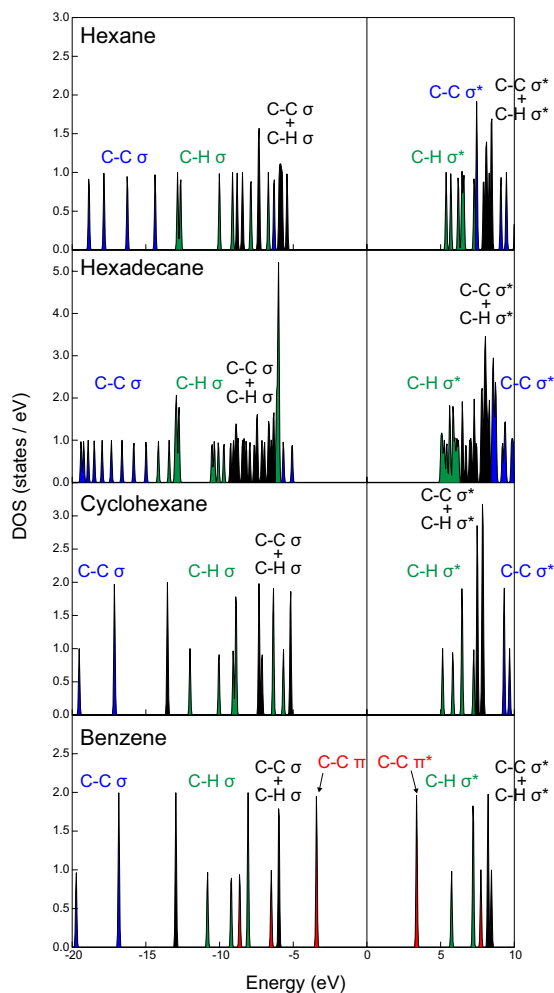
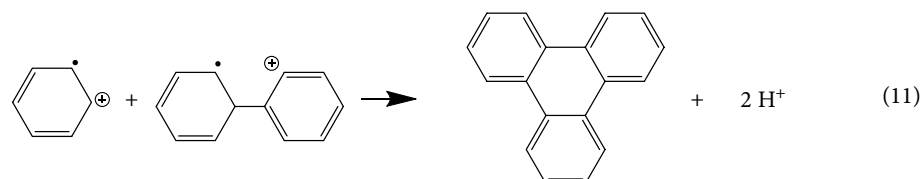
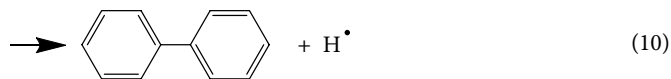
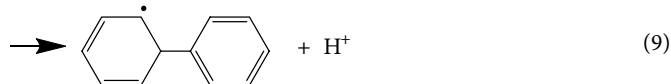
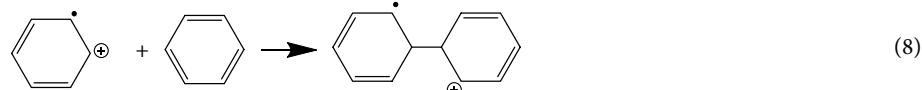
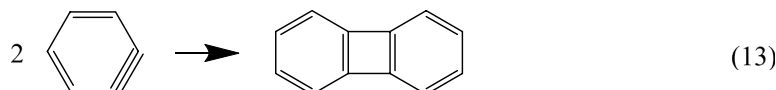


Figure 9. The density of states of hexane, hexadecane, cyclohexane, and benzene. The respective states are divided according to the contribution type of $C-C \sigma$, $C-C \sigma^*$, $C-C \pi$, $C-C \pi^*$, $C-H \sigma$, and $C-H \sigma^*$ orbitals.



In general, the polymerization rate of benzene radical cations is fast; the benzene radical cations are continuously produced at the plasma–solution interface because of the plasma sheath. Moreover, the benzene radical cation is converted into *o*-benzyne and then into biphenylene through reactions (12) and (13):



As previously discussed, the two reaction fields (one in the plasma and the other at the interface) can explain the higher synthesis rate of nanocarbons achieved in the case of benzene.

Conclusion

In this study, we investigated nanocarbon formation routes from hexane, hexadecane, cyclohexane, and benzene via solution plasma. To simplify the possible routes, starting materials categorized as linear or ring molecules were used. GC/MS analysis revealed that the linear molecules were decomposed into shorter olefins, whereas the ring molecules were reconstructed. Saturated ring molecules were polymerized through cation radicals, such as benzene radical cations, and were converted into two- and three-ring molecules. In comparison to nanocarbons obtained from the ring molecules, nanocarbons obtained from the linear molecules exhibited greater crystallinity. This difference is a consequence of different reaction routes. The nanocarbons obtained from linear molecules were synthesized from small molecules, starting from C_2 molecules, through the plasma region—where they were exposed to heat—similar to the pyrolysis synthesis process. By contrast, the nanocarbons obtained from the ring molecules were synthesized through intermediates, such as the benzene radical cations, at the plasma–solution interface, similar to the mechanism encountered in the polymerization. Because of these different routes, the crystallinity of the nanocarbons obtained from the ring molecules was lower than that of the nanocarbons obtained from the linear molecules. To confirm the schemes above, the reactivities of the starting materials were evaluated via *ab initio* MO calculations. In the case of the linear molecules, the primary and secondary reactions are the decomposition of C–C bonds and C–H bonds, respectively. Conversely, in the case of the ring molecules, the primary reaction is the excitation of π -bonds. The secondary reaction is the emission of electrons from molecules, which leads to the formation of cation radicals, which serve as the intermediate to PAHs.

Methods

Carbon nanomaterial samples were prepared using a solution plasma process. Figure 10 shows the experimental setup for the solution plasma and synthesis flow of nanocarbons. A bipolar pulsed power supply (Kurita Co. Ltd., MPS-R06K01C-WP1-6CH) was used to form the solution plasma. The electrodes were tungsten wires with 1 mm diameter. The electrodes were covered with isolated segments of ceramic. The applied peak voltage between the electrodes was about 1700 V, the repetition frequency was 15 kHz, the pulse width was 1.0 μs , and the electrode gap was 0.5 mm. Plasma was characterized by OES using a spectrograph (Ocean Optics Co. Ltd., USB2000+).

The following chemicals were used as starting substances: hexane ($\geq 99\%$; Sigma-Aldrich Co. Ltd.), hexadecane ($>98.0\%$; Kanto Kagaku Co. Ltd.), cyclohexane ($>99.5\%$; Kanto Kagaku Co. Ltd.), and benzene ($>99\%$; Kanto Kagaku Co. Ltd.). These chemicals were used as received for carbon nanomaterials synthesis.

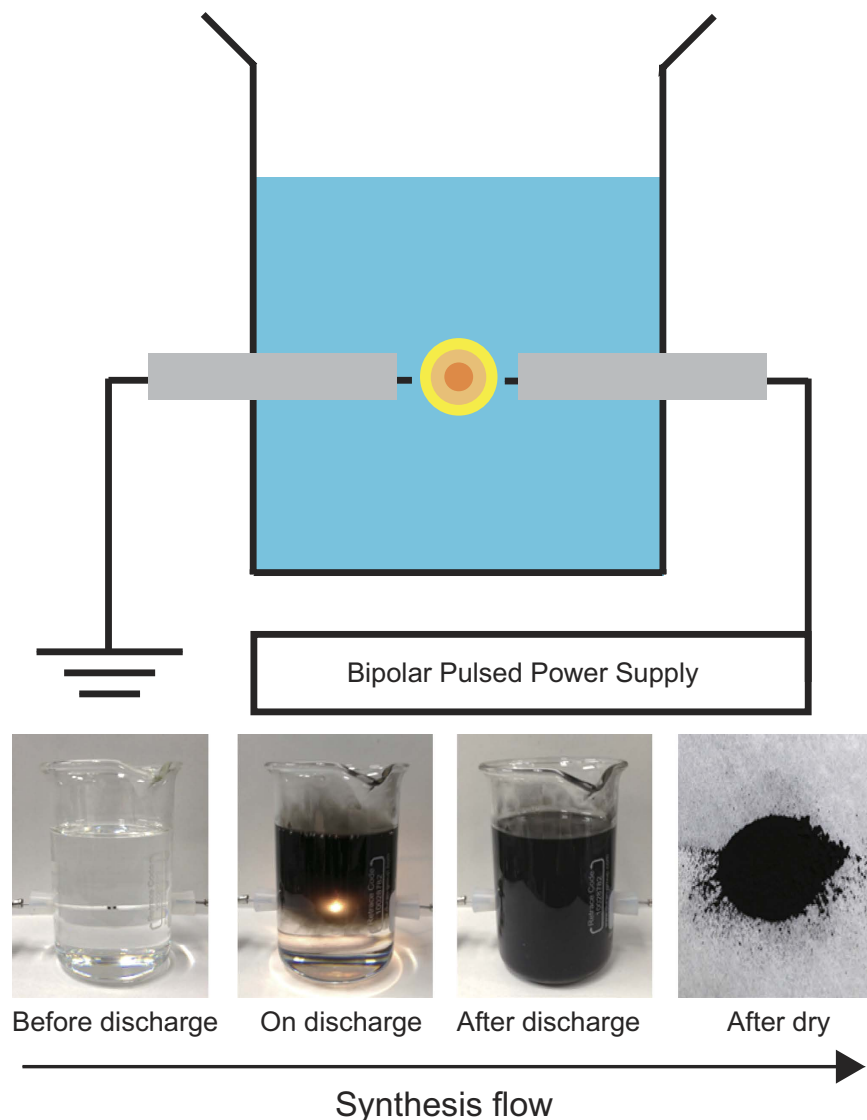


Figure 10. Schematic of the experimental setup for solution plasma experiments and synthesis flow for nanocarbon production.

After the synthesis of the carbon nanomaterials by solution plasma processes, the excess liquids were removed via suction filtration through a membrane filter composed of hydrophilic PTFE having a pore diameter of $0.1\ \mu\text{m}$ (Merck Millipore Co. Ltd., Omnipore JVWP04700). The samples were then completely dried at $100\ ^\circ\text{C}$ in an oven (Yamato Co. Ltd., DX301). The amounts of carbon obtained from each solution with a 250 mL volume during 20 min were measured using a balance (AS-ONE Co. Ltd., EK2000i).

X-ray diffraction (XRD) patterns were recorded using an X-ray diffractometer (Rigaku Co. Ltd., Smartlab) with $\text{Cu K}\alpha$ radiation ($\lambda = 0.15406\ \text{nm}$) operating at 45 kV and 200 mA. Raman spectra were recorded on a spectrometer (JASCO Co. Ltd., NRS-1000) with a laser excitation wavelength of 532 nm.

The intermediate products were confirmed by GC/MS (JEOL JMS-Q1050GC) analysis; the instrument was equipped with a 30-m HP-5 column (Agilent Technologies 19091J-413). Helium was used as a carrier gas for GC at a flow rate of 1.4 mL/min. The column temperature was varied from $40\ ^\circ\text{C}$ to $300\ ^\circ\text{C}$ at a temperature ramp rate of $5\ ^\circ\text{C}/\text{min}$ to $20\ ^\circ\text{C}/\text{min}$. Mass spectrometry was performed for the mass-to-charge ratio range from 20 to 600 m/z . The $1\text{-}\mu\text{L}$ samples were syringed by the splitless injection method at an inlet temperature $350\ ^\circ\text{C}$. Hexane, cyclohexane, and benzene samples were concentrated to ten times by using an oven at $85\ ^\circ\text{C}$ after the treatment.

To investigate the reactivity of the starting materials, we conducted density functional theory calculations using the Gaussian09 software package⁸⁸. B3LYP was applied as an exchange-correlation functional. The basis set adopted for C and H was 6-31G*.

References

- Peter, B. & Christophe, L. Non-thermal plasmas in and in contact with liquids. *J. Phys. D: Appl. Phys.* **42**, 053001 (2009).
- Seiji, S. *et al.* The 2012 plasma roadmap. *J. Phys. D: Appl. Phys.* **45**, 253001 (2012).

3. Locke, B. R., Sato, M., Sunka, P., Hoffmann, M. R. & Chang, J. S. Electrohydraulic discharge and nonthermal plasma for water treatment. *Ind. Eng. Chem. Res.* **45**, 882–905 (2006).
4. Joshi, R. P., Kolb, J. F., Xiao, S. & Schoenbach, K. H. Aspects of plasma in water: streamer physics and applications. *Plasma Process. Polym.* **6**, 763–777 (2009).
5. Andrey, S., Yong, Y., Young, I. C. & Alexander, F. Non-equilibrium plasma in liquid water: dynamics of generation and quenching. *Plasma Sources Sci. Technol.* **20**, 024003 (2011).
6. Nomura, S. *et al.* Microwave plasma in hydrocarbon liquids. *Appl. Phys. Lett.* **88**, 211503 (2006).
7. Lukes, P., Clupek, M., Babicky, V. & Sunka, P. Pulsed electrical discharge in water generated porous-ceramic-coated electrodes. *IEEE Trans. Plasma Sci.* **36**, 1146–1147 (2008).
8. Shinfuku, N. *et al.* Discharge characteristics of microwave and high-frequency in-liquid plasma in water. *Appl. Phys. Exp.* **1**, 046002 (2008).
9. Maehara, T. *et al.* Degradation of methylene blue by RF plasma in water. *Plasma Chem. Plasma Process.* **28**, 467–482 (2008).
10. Ishijima, T., Sugiura, H., Saito, R., Toyoda, H. & Sugai, H. Efficient production of microwave bubble plasma in water for plasma processing in liquid. *Plasma Sources Sci. Technol.* **19**, 015010 (2010).
11. Qiang, C., Junshuai, L. & Yongfeng, L. A review of plasma–liquid interactions for nanomaterial synthesis. *J. Phys. D: Appl. Phys.* **48**, 424005 (2015).
12. Wang, H., Li, J. & Quan, X. Decoloration of azo dye by a multi-needle-to-plate high-voltage pulsed corona discharge system in water. *J. Electrostat.* **64**, 416–421 (2006).
13. Sugiarto, A. T., Ohshima, T. & Sato, M. Advanced oxidation processes using pulsed streamer corona discharge in water. *Thin Solid Films* **407**, 174–178 (2002).
14. Chang, J. S. Recent development of plasma pollution control technology: a critical review. *Sci. Technol. Adv. Mater.* **2**, 571–576 (2001).
15. Saito, N., Hieda, J. & Takai, O. Synthesis process of gold nanoparticles in solution plasma. *Thin Solid Films* **518**, 912–917 (2009).
16. Shirafuji, T. *et al.* Gold nanoparticle synthesis using three-dimensionally integrated micro-solution plasmas. *Jpn. J. Appl. Phys.* **52**, 126202 (2013).
17. Heo, Y. K., Bratescu, M. A., Ueno, T. & Saito, N. Synthesis of mono-dispersed nanofluids using solution plasma. *J. Appl. Phys.* **116**, 024302 (2014).
18. Heo, Y., Bratescu, M. A., Aburaya, D. & Saito, N. A phonon thermodynamics approach of gold nanofluids synthesized in solution plasma. *Appl. Phys. Lett.* **104**, 111902 (2014).
19. Watthanaphanit, A., Panomsuwan, G. & Saito, N. A novel one-step synthesis of gold nanoparticles in an alginate gel matrix by solution plasma sputtering. *RSC Adv.* **4**, 1622–1629 (2014).
20. Hu, X. L., Takai, O. & Saito, N. Synthesis of gold nanoparticles by solution plasma sputtering in various solvents. *JPCS* **417**, 012030 (2013).
21. Bratescu, M. A., Cho, S. P., Takai, O. & Saito, N. Size-controlled gold nanoparticles synthesized in solution plasma. *J. Phys. Chem. C* **115**, 24569–24576 (2011).
22. Hu, X. L., Cho, S. P., Takai, O. & Saito, N. Rapid synthesis and structural characterization of well-defined gold clusters by solution plasma sputtering. *Cryst. Growth Des.* **12**, 119–123 (2012).
23. Hieda, J., Saito, N. & Takai, O. Exotic shapes of gold nanoparticles synthesized using plasma in aqueous solution. *J. Vac. Sci. Technol. A* **26**, 854–856 (2008).
24. Sudare, T., Ueno, T., Watthanaphanit, A. & Saito, N. Accelerated nanoparticles synthesis in alcohol-water-mixture-based solution plasma. *Phys. Chem. Chem. Phys.* **17**, 30255–30259 (2015).
25. Tachibana, K. Current status of microplasma research. *IEEE Trans. Electr. Electr. Eng.* **1**, 145–155 (2006).
26. Banno, M., Kanno, K. & Yui, H. Development of direct gas injection system for atmospheric-pressure in-solution discharge plasma for plasma degradation and material syntheses. *RSC Adv.* **6**, 16030–16036 (2016).
27. Motohiro, B., Kenta, K., Yuu, S. & Hiroharu, Y. Nanosecond time-resolved microscopic spectroscopy for diagnostics of an atmospheric-pressure discharge plasma formed in aqueous solution. *Jpn. J. Appl. Phys.* **54**, 066101 (2015).
28. Xiulan, H., Osamu, T. & Nagahiro, S. Simple synthesis of platinum nanoparticles by plasma sputtering in water. *Jpn. J. Appl. Phys.* **52**, 01AN05 (2013).
29. Hu, X., Shen, X., Takai, O. & Saito, N. Facile fabrication of PtAu alloy clusters using solution plasma sputtering and their electrocatalytic activity. *J. Alloys Compd.* **552**, 351–355 (2013).
30. Shi, J. *et al.* One-step facile synthesis of Pd nanoclusters supported on carbon and their electrochemical property. *Prog. Nat. Sci.: Mater. Int.* **24**, 593–598 (2014).
31. Hu, X. *et al.* One-step facile synthesis of carbon-supported PdAu nanoparticles and their electrochemical property and stability. *J. Alloys Compd.* **619**, 452–457 (2015).
32. Pootawang, P., Saito, N. & Takai, O. Ag nanoparticle incorporation in mesoporous silica synthesized by solution plasma and their catalysis for oleic acid hydrogenation. *Mater. Lett.* **65**, 1037–1040 (2011).
33. Bratescu, M. A., Takai, O. & Saito, N. One-step synthesis of gold bimetallic nanoparticles with various metal-compositions. *J. Alloys Compd.* **562**, 74–83 (2013).
34. Bratescu, M. A. & Saito, N. Charge doping of large-area graphene by gold-alloy nanoparticles. *J. Phys. Chem. C* **117**, 26804–26810 (2013).
35. Panomsuwan, G., Watthanaphanit, A., Ishizaki, T. & Saito, N. Water-plasma-assisted synthesis of black titania spheres with efficient visible-light photocatalytic activity. *Phys. Chem. Chem. Phys.* **17**, 13794–13799 (2015).
36. Hu, X. *et al.* Plasma-induced synthesis of CuO nanofibers and ZnO nanoflowers in water. *Plasma Chem. Plasma Process.* **34**, 1129–1139 (2014).
37. Kim, H. M., Watthanaphanit, A. & Saito, N. Synthesis of colloidal MnO₂ with a sheet-like structure by one-pot plasma discharge in permanganate aqueous solution. *RSC Adv.* **6**, 2826–2834 (2016).
38. Jianbo, Z. *et al.* Synthesis of SnO₂ nanoparticles using a solution plasma and their gas-sensing properties. *Jpn. J. Appl. Phys.* **55**, 01AE17 (2016).
39. Lee, H. S., Bratescu, M. A., Ueno, T. & Saito, N. Solution plasma exfoliation of graphene flakes from graphite electrodes. *RSC Adv.* **4**, 51758–51765 (2014).
40. Hyun, K. Y., Ueno, T., Panomsuwan, G., Li, O. L. & Saito, N. Heterocarbon nanosheets incorporating iron phthalocyanine for oxygen reduction reaction in both alkaline and acidic media. *Phys. Chem. Chem. Phys.* **18**, 10856–10863 (2016).
41. Hyun, K. Y., Ueno, T., Li, O. L. & Saito, N. Synthesis of heteroatom-carbon nanosheets by solution plasma processing using N-methyl-2-pyrrolidone as precursor. *RSC Adv.* **6**, 6990–6996 (2016).
42. Tatsuru, S. *et al.* Functionalization of multiwalled carbon nanotubes by solution plasma processing in ammonia aqueous solution and preparation of composite material with polyamide 6. *Jpn. J. Appl. Phys.* **52**, 125101 (2013).
43. Terashima, C. *et al.* Solution plasma sputtering processes for the synthesis of PtAu/C catalysts for Li-air batteries. *Int J Electrochem Sci* **8**, 5407–5420 (2013).
44. Kang, J., Li, O. L. & Saito, N. A simple synthesis method for nano-metal catalyst supported on mesoporous carbon: the solution plasma process. *Nanoscale* **5**, 6874–6882 (2013).

45. Kang, J., Kim, H. M., Saito, N. & Lee, M. H. A simple synthesis method for nanostructured Co-WC/carbon composites with enhanced oxygen reduction reaction activity. *Sci. Technol. Adv. Mater.* **17**, 37–44 (2016).
46. Yaowarat, W., Li, O. L. & Saito, N. Highly durable silica-coated Pt/carbon nanotubes for proton-exchange membrane fuel cells application. *Jpn. J. Appl. Phys.* **55**, 01AE23 (2016).
47. Prasertsung, I., Damrongsakkul, S. & Saito, N. Crosslinking of a gelatin solutions induced by pulsed electrical discharges in solutions. *Plasma Process. Polym.* **10**, 792–797 (2013).
48. Yaowarat, W., Li, O. L. & Saito, N. Highly durable silica coated Pt/Cs with different surfactant types for proton exchange membrane fuel cell applications. *RSC Adv.* **5**, 44258–44262 (2015).
49. Watthanaphanit, A., Heo, Y. K. & Saito, N. Influence of the discharge time of solution plasma process on the formation of gold nanoparticles in alginate matrix. *J. Taiwan Inst. Chem. Eng.* **45**, 3099–3103 (2014).
50. Pornsunthorntawe, O., Katepetch, C., Vanichvattanadecha, C., Saito, N. & Rujiravanit, R. Depolymerization of chitosan–metal complexes via a solution plasma technique. *Carbohydr. Polym.* **102**, 504–512 (2014).
51. Prasertsung, I., Damrongsakkul, S. & Saito, N. Degradation of β -chitosan by solution plasma process (SPP). *Polym. Degrad. Stabil.* **98**, 2089–2093 (2013).
52. Watthanaphanit, A. & Saito, N. Effect of polymer concentration on the depolymerization of sodium alginate by the solution plasma process. *Polym. Degrad. Stabil.* **98**, 1072–1080 (2013).
53. Shirafuji, T., Himeno, Y., Saito, N. & Takai, O. Generation of three-dimensionally integrated micro solution plasmas and its application to decomposition of organic contaminants in water. *J. Photopolym. Sci. Technol.* **26**, 507–511 (2013).
54. Andreeva, N., Ishizaki, T., Baroch, P. & Saito, N. Rapid sterilization of *Escherichia coli* by solution plasma process. *Jpn. J. Appl. Phys.* **51**, 126201 (2012).
55. Pootawang, P., Saito, N., Takai, O. & Lee, S. Y. Rapid synthesis of ordered hexagonal mesoporous silica and their incorporation with Ag nanoparticles by solution plasma. *Mater. Res. Bull.* **47**, 2726–2729 (2012).
56. Prasertsung, I., Damrongsakkul, S., Terashima, C., Saito, N. & Takai, O. Preparation of low molecular weight chitosan using solution plasma system. *Carbohydr. Polym.* **87**, 2745–2749 (2012).
57. Pootawang, P., Saito, N. & Takai, O. Solution plasma for template removal in mesoporous silica: pH and discharge time varying characteristics. *Thin Solid Films* **519**, 7030–7035 (2011).
58. Panuphong, P., Nagahiro, S. & Osamu, T. Solution plasma process for template removal in mesoporous silica synthesis. *Jpn. J. Appl. Phys.* **49**, 126202 (2010).
59. Janpetch, N., Saito, N. & Rujiravanit, R. Fabrication of bacterial cellulose-ZnO composite via solution plasma process for antibacterial applications. *Carbohydr. Polym.* **148**, 335–344 (2016).
60. Kang, J., Li, O. L. & Saito, N. Synthesis of structure-controlled carbon nano spheres by solution plasma process. *Carbon* **60**, 292–298 (2013).
61. Kim, D. W., Li, O. L. & Saito, N. The role of the central Fe atom in the N4-macrocylic structure for the enhancement of oxygen reduction reaction in a heteroatom nitrogen-carbon nanosphere. *Phys. Chem. Chem. Phys.* **16**, 14905–14911 (2014).
62. Kim, D. W., Li, O. L., Pootawang, P. & Saito, N. Solution plasma synthesis process of tungsten carbide on N-doped carbon nanocomposite with enhanced catalytic ORR activity and durability. *RSC Adv.* **4**, 16813–16819 (2014).
63. Kim, D. W., Li, O. L. & Saito, N. Enhancement of ORR catalytic activity by multiple heteroatom-doped carbon materials. *Phys. Chem. Chem. Phys.* **17**, 407–413 (2015).
64. Panomsuwan, G., Saito, N. & Ishizaki, T. Simple one-step synthesis of fluorine-doped carbon nanoparticles as potential alternative metal-free electrocatalysts for oxygen reduction reaction. *J. Mater. Chem. A* **3**, 9972–9981 (2015).
65. Panomsuwan, G., Saito, N. & Ishizaki, T. Nitrogen-doped carbon nanoparticles derived from acrylonitrile plasma for electrochemical oxygen reduction. *Phys. Chem. Chem. Phys.* **17**, 6227–6232 (2015).
66. Panomsuwan, G., Chiba, S., Kaneko, Y., Saito, N. & Ishizaki, T. *In situ* solution plasma synthesis of nitrogen-doped carbon nanoparticles as metal-free electrocatalysts for the oxygen reduction reaction. *J. Mater. Chem. A* **2**, 18677–18686 (2014).
67. Li, O. L., Hayashi, H., Ishizaki, T. & Saito, N. Enhancement of conductivity in nano carbon balls by the addition of carbon tetrachloride via room temperature solution plasma process. *RSC Adv.* **6**, 51864–51870 (2016).
68. Panomsuwan, G., Saito, N. & Ishizaki, T. Electrocatalytic oxygen reduction activity of boron-doped carbon nanoparticles synthesized via solution plasma process. *Electrochem. Commun.* **59**, 81–85 (2015).
69. Panomsuwan, G., Saito, N. & Ishizaki, T. Electrocatalytic oxygen reduction on nitrogen-doped carbon nanoparticles derived from cyano-aromatic molecules via a solution plasma approach. *Carbon* **98**, 411–420 (2016).
70. Panomsuwan, G., Saito, N. & Ishizaki, T. Nitrogen-doped carbon nanoparticle–carbon nanofiber composite as an efficient metal-free cathode catalyst for oxygen reduction reaction. *ACS Appl. Mater. Interfaces* **8**, 6962–6971 (2016).
71. Hyun, K. Y., Ueno, T. & Saito, N. Synthesis of nitrogen-containing carbon by solution plasma in aniline with high-repetition frequency discharges. *Jpn. J. Appl. Phys.* **55**, 01AE18 (2016).
72. Senthilnathan, J., Weng, C. C., Liao, J. D. & Yoshimura, M. Submerged liquid plasma for the synthesis of unconventional nitrogen polymers. *Sci. Rep.* **3**, 2414 (2013).
73. Maruyama, S. & Yamaguchi, Y. Molecular dynamics demonstration of annealing to a perfect C_{60} structure. *Chem. Phys. Lett.* **286**, 343–349 (1998).
74. Baba, K., Kaneko, T. & Hatakeyama, R. Ion irradiation effects on ionic liquids interfaced with rf discharge plasmas. *Appl. Phys. Lett.* **90**, 201501 (2007).
75. Kaneko, T., Chen, Q., Harada, T. & Hatakeyama, R. Structural and reactive kinetics in gas–liquid interfacial plasmas. *Plasma Sources Sci. Technol.* **20**, 034014 (2011).
76. Sevilla, M. & Fuertes, A. B. The production of carbon materials by hydrothermal carbonization of cellulose. *Carbon* **47**, 2281–2289 (2009).
77. Bohme, D. K., Wlodek, S., Zimmerman, J. A. & Eyler, J. R. Formation of $C_{10}H_8^+$ from the benzene radical cation: a case for the growth of polycyclic aromatic hydrocarbon ions by ion/molecule reactions in the gas phase? *Int. J. Mass Spectrom. Ion Process.* **109**, 31–47 (1991).
78. Momoh, P. O., Abrash, S. A., Mabrouki, R. & El-Shall, M. S. Polymerization of ionized acetylene clusters into covalent bonded ions: evidence for the formation of benzene radical cation. *J. Am. Chem. Soc.* **128**, 12408–12409 (2006).
79. Soliman, A. R., Hamid, A. M., Attah, I., Momoh, P. & El-Shall, M. S. Formation of nitrogen-containing polycyclic cations by gas-phase and intracluster reactions of acetylene with the pyridinium and pyrimidinium ions. *J. Am. Chem. Soc.* **135**, 155–166 (2013).
80. Holman, R. W., Rozeboom, M. D., Gross, M. L. & Warner, C. D. Mass spectrometry for investigations of gas-phase radical cation chemistry. *Tetrahedron* **42**, 6235–6244 (1986).
81. Holman, R. W., Warner, C. D., Hayes, R. N. & Gross, M. L. Reaction of the benzene radical cation with neutral cyclopropane and cyclobutane. *J. Am. Chem. Soc.* **112**, 3362–3368 (1990).
82. Mohan, H. & Mittal, J. P. Pulse radiolysis investigations on acidic aqueous solutions of benzene: formation of radical cations. *J. Phys. Chem. A* **103**, 379–383 (1999).
83. Matsuura, A., Nishinaga, T. & Komatsu, K. Structural studies on the radical cations of benzene, naphthalene, biphenylene, and anthracene fully annelated with bicyclo[2.2.2]octene frameworks. *J. Am. Chem. Soc.* **122**, 10007–10016 (2000).
84. Delaunay, R. *et al.* Molecular growth inside of polycyclic aromatic hydrocarbon clusters induced by ion collisions. *J. Phys. Chem. Lett.* **6**, 1536–1542 (2015).

85. Richter, H. & Howard, J. B. Formation of polycyclic aromatic hydrocarbons and their growth to soot—a review of chemical reaction pathways. *Prog. Energ. Combust. Sci.* **26**, 565–608 (2000).
86. Parker, D. S. N. *et al.* Low temperature formation of naphthalene and its role in the synthesis of PAHs (Polycyclic Aromatic Hydrocarbons) in the interstellar medium. *P. Natl. Acad. Sci.* **109**, 53–58 (2012).
87. Yasukazu, O., Yoshishige, Y. & Tetsuo, O. Dehydrogenation of cyclohexane catalyzed by active carbon. *J. Japan Petrol. Inst.* **22**, 164–169 (1979).
88. Gaussian 09, Revision D.01, Frisch, M. J. *et al.* Gaussian, Inc., Wallingford CT, 2009.

Author Contributions

N.S. and M.A.B. performed the experimental planning, experimental measurements, data examination, and manuscript preparation. T.U., P.G. and J.H. contributed to the experimental setup and data analysis. T.M. and A.Y. contributed to the synthesis, the experimental measurements setup, and *ab initio* MO calculations.

Additional Information

Supplementary information accompanies this paper at <http://www.nature.com/srep>

Competing financial interests: The authors declare no competing financial interests.

How to cite this article: Morishita, T. *et al.* Fastest Formation Routes of Nanocarbons in Solution Plasma Processes. *Sci. Rep.* **6**, 36880; doi: 10.1038/srep36880 (2016).

Publisher's note: Springer Nature remains neutral with regard to jurisdictional claims in published maps and institutional affiliations.



This work is licensed under a Creative Commons Attribution 4.0 International License. The images or other third party material in this article are included in the article's Creative Commons license, unless indicated otherwise in the credit line; if the material is not included under the Creative Commons license, users will need to obtain permission from the license holder to reproduce the material. To view a copy of this license, visit <http://creativecommons.org/licenses/by/4.0/>

© The Author(s) 2016